International Satellite Cloud Climatology Project: Extending the Record

WILLIAM B. ROSSOW,[a] KENNETH R. KNAPP,[b] AND ALISA H. YOUNG[c]

[a] *Franklin, New York*
[b] *NOAA National Centers for Environmental Information, Asheville, North Carolina*
[c] *NOAA Center for Satellite Applications and Research, College Park, Maryland*

ABSTRACT: ISCCP continues to quantify the global distribution and diurnal-to-interannual variations of cloud properties in a revised version. This paper summarizes assessments of the previous version, describes refinements of the analysis and enhanced features of the product design, discusses the few notable changes in the results, and illustrates the long-term variations of global mean cloud properties and differing high cloud changes associated with ENSO. The new product design includes a global, pixel-level product on a 0.1° grid, all other gridded products at 1.0°-equivalent equal area, separate satellite products with ancillary data for regional studies, more detailed, embedded quality information, and all gridded products in netCDF format. All the data products including all input data, expanded documentation, the processing code, and an operations guide are available online. Notable changes are 1) a lowered ice–liquid temperature threshold, 2) a treatment of the radiative effects of aerosols and surface temperature inversions, 3) refined specification of the assumed cloud microphysics, and 4) interpolation of the main daytime cloud information overnight. The changes very slightly increase the global monthly mean cloud amount with a little more high cloud and a little less middle and low cloud. Over the whole period, total cloud amount slowly decreases caused by decreases in cumulus/altocumulus; consequently, average cloud-top temperature and optical thickness have increased. The diurnal and seasonal cloud variations are very similar to earlier versions. Analysis of the whole record shows that high cloud variations, but not low clouds, exhibit different patterns in different ENSO events.

SIGNIFICANCE STATEMENT: This paper reports on the evolution of the research goals and satellite cloud data products produced by ISCCP, a long-term international project, which is now fully operational. The growing length of record with 10-km and 3-h sampling makes possible studies of cloud variations from diurnal-to-weather scale (cloud process scale) to climate variation scale. In particular the length of record includes many examples of ENSO and is beginning to encompass the slower modes of ocean variation, allowing studies of the role of cloud feedbacks in coupling the atmosphere and ocean circulations.

KEYWORDS: Clouds; Cloud cover; Cloud retrieval

1. Introduction

ISCCP was established in 1982 as the first project of the WCRP to 1) organize and modify satellite observations to make them easier to use for cloud research, 2) stimulate research on satellite cloud retrievals, and 3) produce a global cloud climatology to advance understanding of the role of clouds in Earth's radiation budget and hydrological cycle and to improve cloud process representation in climate models (Schiffer and Rossow 1983).

The first objective was accomplished with the production of the ISCCP-B3 radiance dataset. The B3 data provided reduced-volume satellite radiance images sampled at 30 km and 3 h intervals from (almost) all of the operational weather satellites in a common format with Earth-location and satellite view and solar illumination geometry for each image pixel. A common absolute calibration was applied to B3 data to produce ISCCP-BT data, for the infrared window (IR $\sim 10.5\,\mu m$) and visible (VIS $\sim 0.65\,\mu m$) channel radiances (Schiffer and Rossow 1985). Data collection began on 1 July 1983; the B3 data cover the period through December 2009. An additional higher-resolution version of the radiance images, sampled at 10-km and 3-h intervals (called ISCCP-B1), was also collected and continues to this day; the associated location and angle information has been added (this version is called ISCCP-B1U; Knapp 2008b) and calibration refined (called ISCCP-HBT data; Rossow and Ferrier 2015). Figure 1 illustrates the longitude coverage at the equator of the collected B1U data for 1983–2020 from 36 geostationary as well as 15 polar-orbiting satellites.

The second objective—to stimulate cloud research—was achieved by organizing a series of six international workshops from 1982 to 1986 to evaluate available methods for detecting clouds in satellite data (Rossow et al. 1985). The results supported the development of the ISCCP cloud detection method that combined the available approaches (Rossow and Garder 1993a,b; Rossow et al. 1993). This objective also included encouraging improvements in the retrieval of physical cloud properties supported by an international series of field experiments from 1986 to 1994. The results from many of these studies were the basis for a revision of the ISCCP cloud retrievals, especially the introduction of an explicit treatment of ice clouds, to produce a second version of the cloud products, ISCCP-D. Work on this objective continued with the Cloud Assessment by GEWEX (Stubenrauch et al. 2013), which,
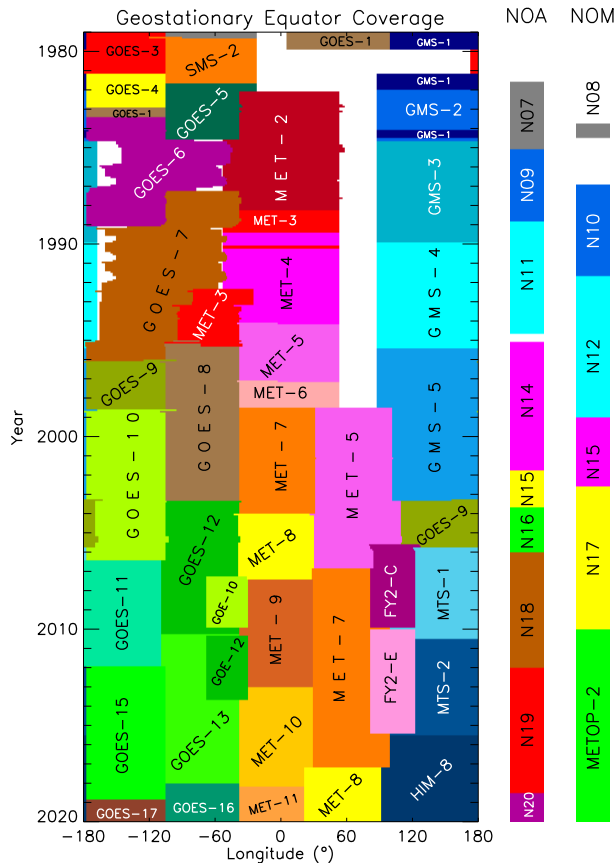
FIG. 1. (left) The variation (in color) with time of the longitude coverage at the equator by individual geostationary weather satellites from 1979 to 2020. (right bars) The corresponding variation in time of polar orbiter coverage in the "afternoon" (NOA) and "morning" (NOM) orbits.

together with results from a number of new satellite instruments flown in the late 1990s and 2000s, formed the basis for a third version of the ISCCP products described here, ISCCP-H.

The third objective—production of a cloud climatology—was fulfilled by producing a dataset that reported cloud amount, top temperature/pressure, and visible optical thickness, together with space–time variation statistics, including cloud-type information and cloud property histograms. The first version of the cloud products, ISCCP-C, was initially released in 1988 and completed in 1992, covering July 1983–June 1991 (Rossow and Schiffer 1991). That the ISCCP cloud products could be used to determine relatively accurate top-of-atmosphere (TOA) and surface radiative fluxes was demonstrated (Zhang et al. 1995; Rossow and Zhang 1995). In the mid-1990s, the radiance calibrations were revised, and the cloud property retrieval model was improved to include a treatment of ice clouds in ISCCP-D, which was first released in 1996 (Rossow and Schiffer 1999) and eventually covered July 1983–December 2009. The improved cloud properties, together with more information about cloud vertical structure (Wang et al. 2000; Rossow et al. 2005a), provided improvements in derived TOA and surface radiative fluxes, together with estimates of flux profiles (Zhang et al.

2004). Initial investigations of cloud processes (hydrological cycle) began, in particular, using Lagrangian compositing (e.g., Machado et al. 1998; Luo and Rossow 2004; Polly and Rossow 2016) and the concept of "weather states" defined by characteristic mesoscale patterns of the joint distributions of cloud-top pressure and optical thickness (e.g., Jakob and Tselioudis 2003; Tselioudis et al. 2013, 2021).

The continued evolution of cloud studies (see section 2c) and advances in satellite cloud measurements has led to a shift of project objectives to emphasize more the study of cloud processes, especially precipitation, and the longer-term climate-scale variations. The former requires increasing the resolution and detail of the cloud products and the latter requires more care to reduce artifacts in the record that is now growing longer than 35 years. To better address these newer goals and to provide for extending the length of record, the third version, ISCCP-H, has been developed and all of the processing made completely operational (Young et al. 2018).

The increase in resolution and detail is made possible by shifting the ISCCP analysis to the ISCCP-B1U radiance collection (Knapp 2008b). This change allows for results to be reported at 1° map resolution instead of 2.5°. The normalization of the radiances to a common standard has been made more statistically robust by enhancing the approach suggested by Inamdar and Knapp (2015). Two new products have been developed, one a global, pixel-level product on a 0.1° equal-angle map grid, more useful for process studies, and the other a gridded version with ancillary data separately for each satellite, more useful for regional or field studies. The time sampling interval of the new products remains at 3 h, but the reengineered processing software is now publicly available and has been designed to allow for processing any version of the same radiance imaging data at any spatial sampling ≤ 30 km and any time sampling interval ≤ 3 h.

Some artifacts in the first two versions of the products (see section 2b) were introduced by inhomogeneities in the ancillary products used in the analysis. Improved record homogeneity (climate quality) of the new ISCCP-H has been achieved by introducing more stringent quality checking of the radiance images and by replacing all of the ancillary products with newer, more uniform, and higher quality products now available that cover the same time period as ISCCP.

To continue ISCCP, and as a pathfinder for building up a global satellite information system (Rossow and Bates 2019), the ISCCP processing has been moved from research-to-operations (R2O). The ISCCP-H products now cover July 1983 through June 2018 and will continue to be produced by the same international cooperation of the operational weather satellite operators (see section 3e) with the product processing being carried out at NCEI. The documentation of the design of the processing system has been extensively updated and improved in detail: the Climate—Algorithm Theoretical Basis Document (C-ATBD; Rossow 2017) and a user's guide are available online (https://www.ncdc.noaa.gov/cdr/atmospheric/cloud-properties-isccp).

This paper describes the new ISCCP-H products (see also Young et al. 2018) in the context of assessments of the previous ISCCP products. Section 2 provides a brief summary of

TABLE 1. Summary of global cloud properties from the ISCCP D version and H version for the periods indicated compared to range of values reported for the 12 data products in the GEWEX Cloud Assessment (Stubenrauch et al. 2012). All parameters are reported averaged over all clouds, for low (L), middle (M), and high (H) clouds regardless of phase and for liquid and ice clouds (liq and ice) regardless of cloud-top pressure. CA are shown relative to the total cloud amount with the absolute values in parentheses. TC are in kelvins, and TAU are unitless. Since the grid-averaged TC and TAU values are interpolated over the nighttime but the cloud-type values are not, averaging over the month produces a difference between the grid-averaged cloud properties and the weighted average of the cloud-type properties. The values of cloud-type properties shown in the table have been scaled to remove this difference.

Property	GEWEX	ISCCP-D	ISCCP-H
	Range	1983–2009	1983–2018
CA	0.61–0.73	0.66 ± 0.015	0.64 ± 0.028
CAH/CA	0.22–0.55	0.33 (0.22)	0.36 (0.23)
CAM/CA	0.11–0.28	0.29 (0.19)	0.28 (0.18)
CAL/CA	0.26–0.42	0.38 (0.25)	0.36 (0.23)
CAliq	0.28–0.72	0.51 (0.34)	0.61 (0.39)
CAice	0.18–0.70	0.49 (0.33)	0.39 (0.25)
TC	248–265	261.5 ± 2.7	260.4 ± 2.0
TCH	222–242	237	226.9
TCM	259–266	262	265.7
TCL	278–282	279	281.7
TCliq	270–280	275	274.6
TCice	220–270	245	225.2
TAU	2.0–9.0[a]	4.0 ± 0.3	4.6 ± 0.4
TAUH	—	2.7	3.4
TAUM	—	4.4	5.4
TAUL	—	4.2	4.6
TAUliq	2.5–9.0	4.4	5.1
TAUice	1.5–10.0	2.7	3.7

[a] The range is reduced to 2.0–6.5 excluding products that averaged values linearly.

evaluations of the ISCCP-D, and section 3 summarizes the changes made to produce the ISCCP-H. Section 4 gives an overview of the new results to emphasize that they represent generally small refinements of the ISCCP-D but to also describe the most notable changes. Section 5 concludes with some comments about the future.

2. Assessments of ISCCP-D

a. General assessments

Rossow and Schiffer (1999) reviewed assessments of ISCCP-C, described results from research, field experiments and other new satellite measurements that led to ISCCP-D, and provided a preliminary evaluation of the ISCCP-D covering the period 1983–97. Doutriaux-Boucher and Seze (1998) provided an early evaluation of the differences between the C and D versions, which mainly reflected both the smaller detection thresholds over land and the effects of treating ice clouds explicitly. Marchand et al. (2010) document the differences of cloud-top height–optical thickness histograms from collocated scenes for especially difficult cloud types (marine stratus under strong temperature inversions, broken cumulus, and thin cirrus overlying low-level clouds) to evaluate the cloud retrievals in ISCCP-D, MISR, and MODIS. Stubenrauch et al. (2013) summarize a much larger report (Stubenrauch et al. 2012) of comparisons of ISCCP-D with 11 other global cloud products, conducted under the auspices of the GEWEX Data and Assessment

Panel [GDAP; formerly the GEWEX Radiation Panel (GRP)]. In Table 1 we list the range of global mean cloud property values from the 12 data products in the GEWEX Assessment, the average ISCCP-D values for 1983–2009, and the averages for the new ISCCP-H for 1983–2018 (which differ little from averages over 1983–2009). The variations of clouds relative to their global averages with location, season, and height of all these data products, generally exhibited better agreement than the global averages, except in the polar regions and where specifically discussed below.

The range of global cloud amounts (CA) among the products in the GEWEX comparison depended mostly on instrument sensitivity, where the smaller values are obtained by the imagers and the upper limit is obtained from the most sensitive detector, the *CALIPSO* lidar (CALIOP) (Winker et al. 2009). CALIOP also finds the most high-level and least midlevel cloud amounts (0.51 and 0.11 relative to total cloud amount, respectively). The sounders find high-level amounts comparable to the lidar; while the imagers (including ISCCP) find more midlevel cloud amount than the sounders and lidar (although the sums of the relative amounts of high- and midlevel clouds are more comparable to the lidar results). All three types of instruments get about the same (absolute) amounts of low-level clouds (see Fig. 1 in Stubenrauch et al. 2013). Different thresholds for identifying cloud phase led to the sounders finding relatively less ice cloud than the imagers, even though the latter have relatively less high-level cloud than the sounders (cf. Fig. 3.2.1 in Stubenrauch et al. 2012). ISCCP-H has slightly more high-level cloud (less middle and

low cloud), but less ice cloud relative to ISCCP-D (because of changed phase temperature criterion, see section 3c). The variations of detection sensitivity and different measurement methods lead to a monotonic relationship of overall average cloud-top temperatures (TC) from coldest for the lidar to warmest for the imagers, with the largest range of the results for high-level clouds. The ISCCP-D and ISCCP-H values of TC are in the upper end of the range; but, because of different atmospheric datasets and methods of determining cloud-top pressure (PC), the PC values tend to be in the lower range of values, especially for lower level clouds. Average cloud optical thicknesses (TAU) for the lidar and sounders are biased low because of their saturation at values greater than about 3, but the range of imager-based values is still large (the range is reduced to 2–6.5 by excluding products that averaged values linearly). The ISCCP-H TAU values for ice clouds are larger than in ISCCP-D (because of corrected errors in the ISCCP-D retrieval, see section 3c). The ISCCP cloud properties have also been evaluated by using them to calculate top-of-atmosphere and surface radiative fluxes, showing very good agreement (Zhang et al. 2004; Raschke et al. 2016). See Stubenrauch et al. (2012, 2013) for more detailed discussion of these comparison results. More recent evaluations of ISCCP-D are discussed in sections 3 and 4.

b. Assessment of record artifacts

The slow, long-term variation of global CA found in the ISCCP results (cf. Fig. 5) required investigation of possible causes related to inhomogeneities in the data record (cf. Fig. 1). The most thorough investigation is reported in appendix 2 of Stubenrauch et al. (2012) covering the possible effects of radiance calibration changes (Stubenrauch et al. 2012, their appendix Fig. 2.2), changes of global coverage (their appendix Fig. 2.3), the ratio of land-to-water sample populations (their appendix Fig. 2.4), changes in the ratio of day-to-night sample populations (their appendix Fig. 2.5), and the cloud effects of changing satellite view angles (the effects of the gaseous atmosphere are incorporated in the cloud detection algorithm, Rossow and Garder 1993a)—see below. None of these effects is quantitatively large enough to explain all of the global mean variations.

Evan et al. (2007) state in their abstract that "trends observed in the ISCCP data are satellite viewing geometry artifacts and are not related to physical changes in the atmosphere." However, the changes in satellite view angle over time do not explain *all* of the long-term "trend" of global monthly mean CA in the ISCCP record as illustrated in Fig. 2, which shows the average CA and cosine satellite view-angle (MUE) anomaly records averaged over the part of the globe with *any* view-angle changes at any time (Fig. 2a) and over the part of the globe with no view-angle changes in the whole record (Fig. 2b), each roughly half of the total [see Figs. 2.6 and 2.7 in appendix 2 of Stubenrauch et al. (2012) that explain how this division was done]. The portion of the globe involved in a change at any particular time is typically only 10%–20%, so the abrupt CA changes caused by MUE changes from one month to the next do not appear in the full record of CA. A similar pattern of variation of average cloud amount is apparent in both regions, even in the regions with no

changes of satellite view angle. In other words, the MUE changes distort the signal, making the peak value in 1987 larger by about 0.01, for instance, but do not cause all of the signal. Note particularly, there are no significant or systematic view-angle changes after 1998.

We also note a recent comparison of ISCCP-H with three other datasets, all based solely on AVHRR measurements, where these other datasets all show an overall decreasing trend in global mean cloud cover similar to, but smaller than ISCCP (Karlsson and Devasthale 2018). Otherwise, these products all show similar seasonal amplitude and phase except in the polar regions, where there is no agreement (but see section 4b, which compares ISCCP to *CloudSat–CALIPSO* in the polar regions).

Rossow and Garder (1993b) proposed that the view-angle effect was caused by the presence of high-level, optically thin clouds, which are better detected by ISCCP at slant view than nadir view and quantified the magnitude of this effect. Rossow and Schiffer (1999) summarized the evidence for the presence of such clouds from measurements by SAGE and High Resolution Infrared Radiation Sounder (HIRS). Subsequent observations by CALIOP (Naszaryan et al. 2008) have confirmed the presence of this type of cloud that is underreported by ISCCP (Stubenrauch et al. 2013). It can be shown by using pairs of geostationary satellites viewing the same locations at the same time with different view angles that the magnitude of difference in cloud amount detected is proportional to the difference in view angle and to the detected amount of cirrus (Fig. 22 in Rossow 2017). The angle dependence effect has not changed in ISCCP-H though recent work investigates approaches to mitigate the effects by removing optically thinner clouds (Knapp et al. 2021).

Another bias in ISCCP-D results, as mentioned above and pointed out by Stubenrauch et al. (1999) and Marchand et al. (2010), is a tendency for PC values for lower-level clouds to be too small by ~50 hPa, even though the TC values are in good agreement with other measurements (cf. Fig. 3.1.5 in Stubenrauch et al. 2012). This bias is also present in ISCCP-H. The cause is, in part, the atmospheric temperature profile data used to convert TC to PC (cf. Stubenrauch et al. 1999); both the earlier atmospheric dataset and the new one [neural network HIRS (NNHIRS), see section 3d] appear to be slightly too warm in the lower atmosphere by about 2 K, especially when low-level temperature inversions are present. When the temperature profile exhibits a surface inversion, the ISCCP procedure places cloud top at or above the maximum temperature level. In the comparison by Karlsson and Devasthale (2018) it is notable that the ISCCP PC results agree much better with these other datasets if no correction is made for IR radiation transmitted through the clouds from below. In the case of highly broken cloudiness, where the optical thickness of the clouds might be underestimated, this correction could be overestimated; but this difference may also indicate differences of cloud microphysics assumed in the retrievals.

There is also a small overall downward trend (about 15 hPa from 1983 to 2010) in the ISCCP results, stronger in D than H, but the other (diurnally aliased) datasets in Karlsson and Devasthale (2018) all show a positive trend. The ISCCP PC trend appears to be
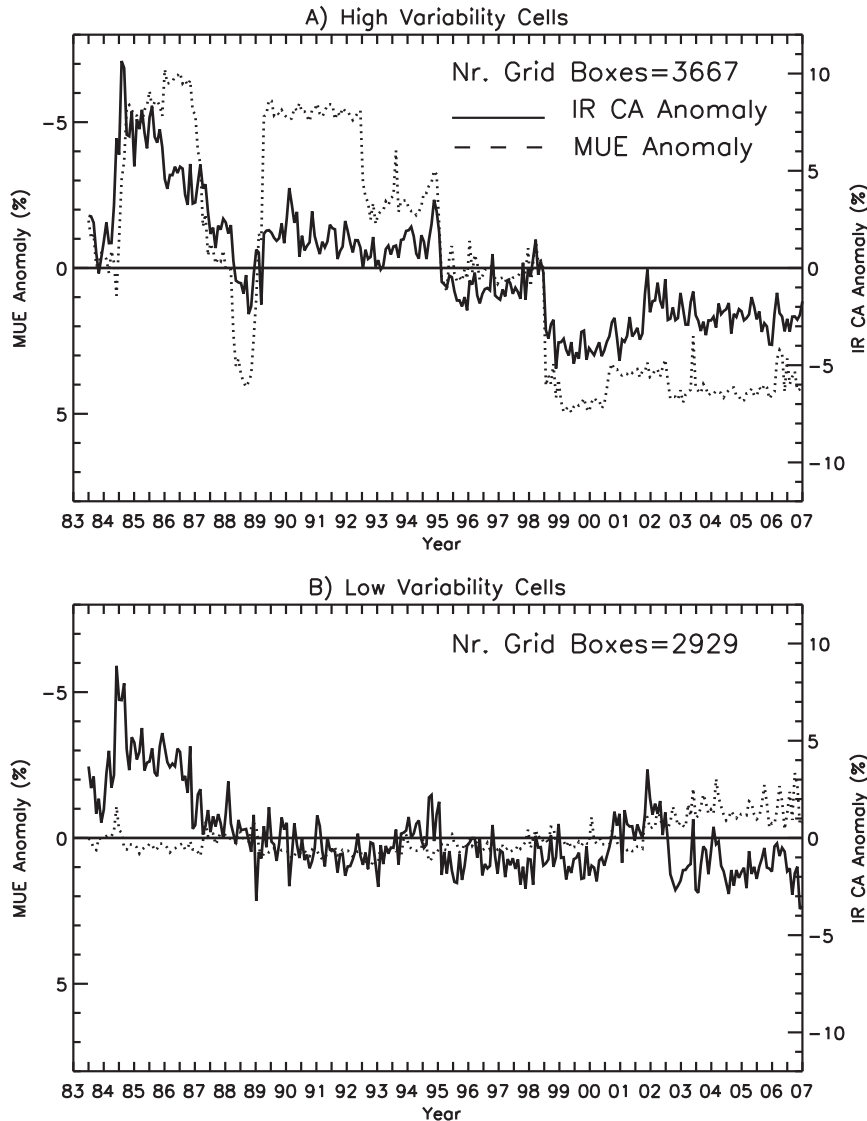
FIG. 2. The effect of changing satellite view angles on the ISCCP-D long-term record of global, monthly mean (deseasonalized) anomalies of cloud amount is shown by averaging the cloud amount anomalies (solid line; %; right scale) and the anomalies of MUE (dashed line; %; left scale) over regions (a) with and (b) without view-angle changes at any time in the record. These regions are held constant over the whole record. The number of map grid cells for each type of region is indicated, however, the fractional area of the globe involved in a change at any time is much smaller.

caused by a negative trend over three decades in the lower atmosphere temperature by about 1 K below the 800 hPa level in the NNHIRS dataset (temperatures and humidities at other levels appear generally stable over the record except for the earliest decade). There is also a decrease in upper level temperatures in the first 18 months of the NNHIRS record, but a decline in TC means that PC does not change much; an increase in PC later in the record (see section 4b) is not associated with any changes in NNHIRS air temperatures. These temperature anomalies are associated with relative humidity (RH) anomalies of 2%–5% and a small decrease of midlevel clouds.

The new ozone product appears to have a larger global mean value by about 5–10 Dobson units in the first decade than in the rest of the record.

One other artifact in ISCCP-D was a sudden increase of surface temperatures by 1–2 K (on average) in about 2000; this was related to a small bias in the IR calibration for the new AVHRR-3 (cf. Knapp 2008a), which has been corrected in ISCCP-H.

c. Assessment by usage

Another way to evaluate the quality of the ISCCP products is by whether they provide useful research results, so we

summarize here for several topics the earliest and latest uses along with some significant results.

The earliest study of diurnal cloud variations was by Fu et al. (1990), who examined the variations of tropical deep convection; the latest study is by Worku et al. (2019), who examined the diurnal variations of clouds and associated precipitation over the tropical Maritime Continent. The earliest most general (global) study of diurnal variations of high and low clouds was by Cairns (1995) (see also section 4b).

The earliest study of tropical deep convection was by Fu et al. (1990), who examined the association of convection with SST and surface wind divergence, and the latest study is by Jakob et al. (2019), who evaluate whether radiative–convective equilibrium holds as a function of space–time scales. Notable results were presented by Machado et al. (1998), who developed tracking of convective systems to study their life cycles, by Rossow et al. (2005b), who extended the analysis of weather states by Jakob and Tselioudis (2003) to the whole tropics over the whole ISCCP record, emphasizing the occurrence of two distinct kinds of deep convection, and by Tan et al. (2015), who found that observed trends in tropical precipitation are explained by trends in only one of the two kinds of deep convection.

Clouds in extratropical cyclones were first looked at by Tselioudis et al. (2000), who quantified the cloud properties and their radiative effects as a function of storm strength, and most recently by Polly and Rossow (2016), who detailed the climatology of radiation and precipitation with storm types defined by size and strength. Haynes et al. (2011) determined the distinctive patterns of clouds within southern extratropical cyclones, extending the results of Lau and Crane (1995).

The earliest examination of the seasonal cycle of cloud properties was a global analysis by Rossow et al. (1993). Zhang et al. (2005) conducted a multimodel evaluation against observations; the latest study (Karlsson and Devasthale 2018) compared several satellite observations of seasonal cloud variations (see also Stubenrauch et al. 2013).

A variety of phenomena in the tropics have been studied using ISCCP products. Aspects of the Asian monsoon have been examined ranging from Drake (1993) to Zhang et al. (2020). Especially detailed studies over Darwin, Australia, have been carried out in a series of papers, starting with a regime diagnosis in Pope et al. (2009a,b). The effect of the MJO on the diurnal variations of convection was studied by Tian et al. (2006) using the variations of satellite IR radiance features; a much more complete diagnostic study of MJO events was performed by Tromeur and Rossow (2010), who identified a characteristic switching of convective organization at the onset of the phenomenon. The latest study of the MJO by Worku et al. (2020) extended the studies of Tian et al. (2006) and Tan and Jakob (2013) to document how the diurnal variation of deep convection over the Maritime Continent interacts with MJO events. The initiation of African easterly waves has been shown to be associated with the same switching of convection organization by Mekonnen and Rossow (2011, 2018). The earliest study of tropical cloud variations in ENSO events was performed by Rossow and Cairns (1995). Zhang et al. (2007) drew attention to the differences of the pattern of poleward heat transport in different ENSO events (see section 4b).

Tselioudis et al. (2010) and Sun and Huang (2018) have connected variations in tropical deep convection with decadal changes in stratospheric water vapor. Tselioudis et al. (2016) have identified trends in high clouds that suggest changes in the latitudinal extent of the Hadley circulation.

The earliest diagnoses of cloud properties and radiative fluxes at the TOA were by Darnell et al. (1992) and Hartmann et al. (1992), the latter dividing the effects by cloud type. Gupta et al. (1999) presented the early global results of the international Surface Radiation Budget project (SRB) that uses ISCCP products to calculate top-of-atmosphere and surface radiative fluxes. Chen et al. (2000) extended the diagnosis of cloud-type effects to both the TOA and surface fluxes. Zhang et al. (2004) produced globally extensive estimates of radiative flux profiles; these results were recently extended to ISCCP-H (called ISCCP-FH, see Zhang_etal_flux-cal_at-isccp_v4_2021.pdf under "FH Documentation and Publications" at https://isccp.giss.nasa.gov/projects/flux.html). Oreopoulos and Rossow (2011) quantified the analysis of TOA and surface fluxes by different cloud regimes. Tselioudis et al. (2013) determined global cloud regimes (weather states) and showed their association with cloud vertical structures and the large-scale atmospheric circulation.

The earliest connection of cloud properties and precipitation was by Lin and Rossow (1996). Jakob and Schumacher (2008) quantified the separate contributions to tropical precipitation from the tower and anvil components. Luo et al. (2017) combined TRMM, *CloudSat*, *CALIPSO*, and ISCCP to document the vertical cloud and precipitation structures of tropical convection.

3. D-to-H version changes

a. Radiance calibration and quality control procedures

Several assessments or comparisons of the ISCCP VIS radiance calibration have been made since 1999 (see Rossow and Ferrier 2015 for discussion and references). Particularly important were studies that calibrated all of the AVHRR instruments, solar bands (Heidinger et al. 2010), and infrared (Cao and Heidinger 2002), anchored on the calibration of MODIS (called the PATMOS-x calibration). Since the original anchor for the ISCCP calibration was *NOAA-9* (aircraft-based VIS for 1985–88) very far in the past, Rossow and Ferrier (2015) adopted a compromise VIS calibration using both *NOAA-9* and *NOAA-18* (MODIS-based for 2006–09) as anchors. *NOAA-19* is currently the reference satellite. Inamdar and Knapp (2015) conducted an independent normalization of the geostationary satellite VIS calibrations to the AVHRRs with the PATMOS-x AVHRR calibrations. Knapp (2008a) showed by comparison to HIRS onboard the same satellites that there is a discontinuity in the ISCCP IR calibration between AVHRR-3 and the earlier models. For ISCCP-H, the updated solar spectrum dataset and instrument spectral response functions, recommended by Molling et al. (2010), have been used and a compromise VIS calibration developed by Rossow and Ferrier (2015) adopted. A small correction to the

IR calibration for *NOAA-15* through *NOAA-19* was also applied (Rossow 2017). For ISCCP-H processing, the normalization procedure has been fully automated using statistics derived directly from all collocated AVHRR and B1U data themselves rather than samples as before. The final postprocessing inspections comparing geostationary results shows that the *precision* of the calibration normalization and postprocessing procedures is limited to about 2% absolute for the VIS and about 1.0 K for the IR (see Rossow 2017 for more details).

b. Cloud detection

The changes made to the ISCCP-D cloud detection procedure for ISCCP-H are small refinements, with the exception of changes in the polar regions, as follows: 1) The smaller spatial sampling interval of the ISCCP-B1U radiance data is exploited by performing the space-contrast tests (cf. Rossow and Garder 1993a) in smaller subdomains that divide land and water areas within original test domains that were mixtures (about 15% of the globe). 2) The surface type categories that set the test parameters used in the algorithm tests have been updated and some changes in thresholds made. IR thresholds were decreased by 0.5 K to 3.0 K over coastal water, by 1.0 K to 3.0 K near or over sea ice, and by 1.0 K to 5.0 K over rough or high topography. VIS thresholds were decreased to 3.0% over coastal water to be the same as open water, to 4.0% over sea ice and 4.5% near sea ice edges (the threshold change for sea ice edges was actually an increase), to 5.0% over land, to 6.0% over snow and 6.5% near snow edges, and to 7.5% over rough or high topography. These very small changes are based on evidence of cloud contamination of ''clear'' radiances in certain locations and the underdetection of cirrus documented in the GEWEX Cloud Assessment (Stubenrauch et al. 2012). As Table 1 shows, there are no significant changes in global mean total or type cloud amounts; the most noticeable changes (but still small) are in the polar regions.

Testing of the ISCCP-D cloud detection algorithm over Arctic sea ice became possible with the availability of a year of surface-based observations from the SHEBA experiment in 1998, especially measurements by a surface-based cloud lidar (Intrieri et al. 2002) and measurements of surface and near-surface atmospheric temperature profiles (see references in Stramler et al. 2011). The SHEBA-based evaluation showed that the ISCCP algorithm tended to miss some clouds in daytime and to reverse the clear-cloudy distinction in nighttime. When lower level clouds are present with near-surface temperature inversions, the ISCCP-D values of TC are closer to the surface temperature (in clear conditions) and the values of surface temperature (TS) are closer to the actual cloud-top temperatures (in cloudy conditions). Later comparisons with CALIOP (Winker et al. 2009), with and without clouds with TAU < 0.3, allowed evaluations over land and water at both poles in all seasons. The GEWEX Assessment (Stubenrauch et al. 2012) showed that, relative to the global annual mean, the ISCCP and CALIOP cloud amounts agreed well: since the CALIOP global annual mean cloud amount is about 0.1 larger than the ISCCP value, this indicated that the ISCCP-D results are still an underestimate (even in winter). Consequently the

ISCCP-H algorithm was changed as follows: 1) the 3.7-μm tests were eliminated because this channel is not available uniformly over the whole record, especially for ''daytime'' conditions, 2) the VIS thresholds over snow and ice were reduced and the IR threshold over sea ice was reduced, and 3) the IR threshold classification of pixels in wintertime (no VIS) was changed to reflect the reversed brightness temperature contrast of some clouds in near-surface temperature inversions. The latter is accomplished by changing the ''marginally cloudy'' category to clear and ''marginally clear'' category to cloudy. The smaller VIS and IR thresholds reduced the CA low bias in summer over the Arctic by about 0.01–0.02, but only partially offset the ≈0.05 decrease in cloud amount over Antarctica in summer produced by eliminating the 3.7-μm tests. Average wintertime Arctic and Antarctic cloud amounts changed by <0.01 (see further discussion of ISCCP-H polar cloud results in section 4b).

c. Retrieval models

The changes made to the radiative transfer calculations that underlie the cloud and surface property retrievals and the retrieval procedure include four corrections of the ISCCP-D retrievals, four significant improvements and seven relatively minor refinements.

Three corrections of the ISCCP-D cloud retrievals affected ice clouds. There were two flaws in the lookup tables used to retrieve ice cloud optical thicknesses, one that produced a gap in the distribution of values near values of 2 and one that restricted values to less than about 50 for more extreme solar illumination geometries, mostly at high latitudes. These flaws have been removed causing, in part, the increase in ice cloud TAU seen in Table 1. The other correction concerned the placement of ice clouds that are so thin as to be detected only by the IR tests. In this case, the VIS-based retrieval of optical thickness gives a value too small to be consistent with smallest atmospheric temperature at the tropopause. The original intention was to place such clouds at the tropopause and calculate a consistent optical thickness; however, in the ISCCP-D code, these clouds were assigned a cloud-top temperature 5 K colder than the tropopause (cf. Fig. 3.1.9 in Stubenrauch et al. 2012 showing a peak in tropical TC colder than the lidar values, especially over land). In ISCCP-H these clouds are now placed at the tropopause temperature/pressure, consistent with the CALIOP results. A fourth correction affected extremely large surface temperatures: the ISCCP-D retrieval code incorrectly used the retrieved surface *skin* temperature to determine the temperature-dependent water vapor IR absorption in the lowest atmospheric layer instead of the surface *air* temperature, which caused an overestimate of TS especially at larger satellite view angles; this has been corrected in ISCCP-H.

The four more significant changes are as follows: 1) added a treatment of the effects of stratospheric and tropospheric aerosol scattering/absorption that was previously neglected for ISCCP-C and D; 2) added a treatment of cloud-top location when near-surface temperature inversions are present (the new ancillary data product has such inversions); 3) changed the cloud-top temperature value used to identify ice phase clouds from 260 to 253 K based on POLDER-MODIS results (Riedi et al. 2010; Coopman et al. 2020), which caused the decrease in

the relative ice cloud amount and (in part) the ice cloud TC seen in Table 1; and 4) updated the ice cloud scattering phase function to an empirically based model from POLDER results (Baran and Labonnote 2007), which reduces systematic angle-dependent biases, and revised the IR/VIS optical thickness ratio. The empirical ice scattering model does not explicitly assume a particle size; however, based on the GEWEX Assessment (Fig. 3.2.9 in Stubenrauch et al. 2012), ISCCP-H calculates ice cloud water path (WP; g m^{-2}) using a specified ice particle effective radius of 20 μm for clouds with TAU < 3.55 and 34 μm for clouds with TAU ≥ 3.55 (which gives an approximate global mean value of 27 μm, the GEWEX range is 23–32 μm), instead of 30 μm used for all ice clouds in the ISCCP-D.

The seven minor refinements are (see Rossow 2017 for details) as follows: 1) replaced the ocean VIS reflectance model with a more accurate version that has an explicit glint treatment (Chowdhary et al. 1995); 2) replaced a single all-satellite value of ozone absorption with more accurate, instrument-specific absorption coefficients; 3) updated the solar ephemeris to epoch 2000; 4) revised the specified liquid cloud droplet effective radius from 10 μm globally to 13 μm over land and 15 μm over ocean, based on the GEWEX Assessment results (cf. Fig. 3.2.8 in Stubenrauch et al. 2012); 5) introduced an explicit cloud layer thickness specification, based on observed humidity layer thicknesses from radiosondes (Wang et al. 2000) and cloud layer thicknesses from CloudSat–CALIPSO (Mace et al. 2009), including gas inside the cloud layer; 6) added water vapor above the 300-hPa level in the atmospheric ancillary data (which does not affect the cloud and surface retrievals but is important for determining radiative fluxes); and 7) improved surface temperature retrievals by accounting for variations of surface IR emissivity by surface type (which changes the result from a surface brightness temperature to a physical temperature that is generally only a few degrees larger, except over deserts).

d. Ancillary data

All ancillary products were replaced in ISCCP-H with more up-to-date versions, in particular new atmospheric temperature–humidity profiles (see appendix D in Rossow 2017 for details of original data sources, references and preprocessing). The new ancillary products are all in 1°-equivalent equal area grids (unless otherwise noted) and include the following: 1) TOPO provides a land–water mask and topographic height (mean and standard deviation) at various grid intervals from 1 to 100 km; 2) SURFACETYPE provides classification of the land surface by vegetation type or glacier cover or open water or permanent ice cover; 3) SNOWICE provides daily sea ice coverage, including permanent ice shelves, and daily snow cover, including permanent glaciers; 4) OZONE provides global daily total column ozone abundances; 5) AEROSOL provides global monthly stratospheric and tropospheric aerosol optical depth and tropospheric fine fraction, based on MACv.1 (Kinne et al. 2013); and 6) NNHIRS provides global, 3-h profiles of temperature and relative humidity up to the 10-hPa level with explicit treatment of surface air temperature–humidity and near-surface temperature inversions (Young et al. 2018 provide references for the ancillary source data).

The NNHIRS product was compared to AIRS and ERA-Interim (ERA-I) products globally and additionally to the Analyzed RadioSoundings Archive, version 2 (ARSA from LMD available at https://ara.lmd.polytechnique.fr/index.php?page=arsa), radiosonde-based product over land. The near-surface temperatures over land were adjusted by comparison to the Integrated Surface Data (ISD) surface-measurement-based product (see Fig. D.1.1 in Rossow 2017); the near-surface relative humidity over oceans was adjusted by comparison to SeaFlux values (Clayson et al. 2012) (see Fig. D.1.2 in Rossow 2017).

Over ocean the average differences between both AIRS and ERA-I and NNHIRS atmospheric temperatures (TA) are from about +0.5 to +1.5 K, except below the 800-hPa level and near the surface where they are from about −0.5 to −1.5 K (positive difference indicates colder NNHIRS values). The average space–time correlations are 0.97–0.99. The differences at the surface could be due to the difference between conventional bulk SST values and the diurnally corrected surface skin temperatures in the SeaFlux product (Clayson and Bogdanoff 2013). The AIRS temperatures are in better agreement with NNHIRS in the polar regions than the ERA-I values. Both AIRS and ERA-I are colder than NNHIRS by 1–3 K near the tropopause and in the stratosphere in the tropics and in the winter polar regions.

Over land the NNHIRS values of TA are a little larger than AIRS and ERA-I by 0.75–2 K at upper levels and near the surface and smaller at midlevels. The average space–time correlations are a little lower, 0.90–0.99. Agreement among all the datasets is slightly better in July than January. Over the summer poles, AIRS and ERA-I are 3 K warmer/cooler (south/north) than NNHIRS at the surface decreasing to about zero difference at 100 hPa; over the winter poles AIRS, ERA-I, and ARSA are 4–5 K warmer than NNHIRS near surface but 1–2 K cooler above the 400-hPa level. Compared to ISD the NNHIRS near-surface values of TA are within 1–2 K except they are colder by about 3 K in both polar regions in winter.

The specific humidity (QA) comparison over oceans (not shown because differences in g kg^{-1} are small), the average differences with AIRS and ERA-I are about −10% (roughly −1.0 g kg^{-1}) at the surface and about +30% aloft. The average space–time correlations range from 0.93 to 0.99. These differences are of the same order as the reported uncertainties in all of the datasets. Relative to NNHIRS at all latitudes in both seasons, AIRS and ERA-I grow progressively wetter than NNHIRS at lower levels, but are drier at the surface, where NNHIRS agrees better with SeaFlux values (because of the adjustment).

Over land the differences are similar to or a little larger than over oceans. The average space–time correlations range from 0.80 to 0.95. Again, the AIRS and ERA-I, as well as ARSA, profiles grow progressively wetter than NNHIRS at lower levels. At the surface AIRS and ERA-I values of QA are in better agreement with ISD values, whereas NNHIRS values are drier than ISD. See appendix D in Rossow (2017) for more details.

e. Changes to go operational

Some parts of the ISCCP-D code dated from 1982 when the ISCCP processing was done on mainframe-style computers.

TABLE 2. Chronology of ISCCP data collection and processing centers.

SPC for Europe/Africa sector	ESA (1983–95)	EUMETSAT (1995–current)
SPC for Indian Ocean sector	IMD[a] (1986)	EUMETSAT (1998–current)
SPC for Southeast Asia sector	CMA[b] (2005–09)	
SPC for East Asia sector	JMA (1983–current)	
SPC for east Pacific sector	CSU[c] (1983–2008)	NOAA (2008–current)
SPC for America sector	UWS[d] (1983–84)	MSC (1987–2008)
	CSU (2008–11)	INPE[e] (2008–10?)
	NOAA (2011–current)	
SPC for afternoon polar orbiter	NOAA (1983–current)	
SPC for morning polar orbiter	NOAA (1983–2010)	EUMETSAT (2010–current)
SCC	MétéoFrance (1983–2009)	NOAA (2016–current)
GPC	NASA GISS (1983–2016)	NOAA (2016–current)
ICA[f]	NOAA (1983–current)	

[a] Indian Meteorological Department.
[b] China Meteorological Administration.
[c] Colorado State University.
[d] University of Wisconsin.
[e] Instituto Nacional de Pesquisas Espaciais.
[f] International Central Archive center.

For the transition to operational processing, the code was thoroughly updated to remove system-specific code features and to make it more modular for portability. The ISCCP-H code has been successfully run on four different operating systems. The other notable changes made to the processing system were 1) addition of ancillary preprocessing programs; 2) addition of extensive quality checking (QC) procedures for all inputs, at intermediate processing stages and at the output of the analysis; and 3) creation of diagnostic programs that can be used to investigate possible problems (see Rossow and Bates 2019).

The cloud detection portion of the code has two important alternate features. The code can be applied (with minimal changes) to any version of the same satellite radiance image data for any space–time sampling intervals smaller than the original ISCCP-B3 data (30 km, 3 h); that is the cloud detection algorithm can be run at any finer resolution (the retrieval step is performed for individual image pixels requiring no changes). The cloud detection algorithm can also be configured to run in near–real time by collecting statistics on a sliding prior-30-day window rather than in a fixed month. The operational version of the ISCCP analysis software is available to the public along with a complete operations guide for setting up and running it online (https://www.ncdc.noaa.gov/cdr/atmospheric/cloud-properties-isccp). The required inputs are calibrated radiance images (single images cannot be analyzed as the cloud detection algorithm requires one month of statistics) and the ancillary products mentioned in section 3d (the cloud detection portion can be run on uncalibrated images). See the C-ATBD and operations guide (appendix E) for more details (Rossow 2017).

Table 2 shows the chronology of the participating data centers for ISCCP. Currently, NCEI serves as the Global Processing Center/Satellite Calibration Center (GPC/SCC) and Sector Processing Center (SPC) for polar orbiters and GOES satellites, EUMETSAT serves as the SPC for Meteosat over Europe/Africa and the Indian Ocean, and JMA serves as the SPC for the Himawari satellites.

4. ISCCP-H product description and some illustrative results

a. Product description

Young et al. (2018) list all of the ISCCP-H products and their equivalents in ISCCP-D for reference. All of the ISCCP-H products, except HXS (the Level 2 product by satellite), are in netCDF4.0 format. In ISCCP-D, some interpolation over time (and a little over space) was applied to the monthly averaged products to fill in missing results or correct for undersampling of the diurnal cycle. In ISCCP-H, these procedures are applied to the global 3-h HXG and HGG products (see details in C-ATBD and user's guide). In particular in the HGG product, grid-average nighttime CA and TC/PC are adjusted based on daytime differences of these quantities between VIS/IR and IR retrievals and TAU/WP are interpolated over the nighttime periods. In addition, the 18 daytime cloud-type amounts, but not their properties, are interpolated over the nighttime. Since the grid-averaged TC and TAU values are adjusted/interpolated over the nighttime, but the cloud-type values are not, averaging over the month (HGH, HGM) produces a difference between the grid-averaged cloud properties and the weighted average of the cloud-type properties, as noted in the caption to Table 1. Because of the removal of near-coastal pixels, the FILL procedures fail in 10 grid cells, mostly in the Maritime Continent area, where there is a too fine a mixture of ocean and land (e.g., the Philippines and also southern Chile).

b. Some new results

The differences among the versions of the ISCCP products are generally small except for some specific features: land cloud amounts increased from ISCCP-C to ISCCP-D, and their vertical location shifted (Doutriaux-Boucher and Seze 1998) because of reduced detection thresholds over land and the introduction of an explicit treatment of ice clouds (Rossow and Schiffer 1999). The differences between ISCCP-D and ISCCP-H are also small (Table 1) except for a decrease of the ice–

liquid cloud amount ratio, thin cirrus locations, polar region cloud properties and a decrease of day–night contrasts as discussed below. The larger-scale or larger-magnitude cloud variation features are very similar (global and regional seasonality of CA and PC are very similar to other products shown by Karlsson and Devasthale 2018 except in the polar regions): general-scale analyses remain valid (cf. a global analysis by Rossow and Cairns 1995). The introduction of a treatment of aerosol effects did not change the results much (except for periods where volcanic aerosols are prevalent) because the radiative effects of aerosols were included implicitly in the ISCCP-D surface reflectivity. Rather than show previous results using ISCCP-H, we summarized the literature of cloud variation studies using ISCCP products in section 2c.

The cloud amount frequency distribution in the higher-spatial-resolution ISCCP-H is even more "U shaped" (more zeros and ones) than for ISCCP-C and D (cf. Rossow et al. 1993) as expected because of the smaller map grid size; the distribution now more closely resembles the distribution from surface-based observations with somewhat more frequent 0.9–1.0 cover than the surface observations, which miss some of the thinner cirrus.

Overall (Table 1), the ISCCP-H cloud amounts differ from ISCCP-D by less than 0.01, except for the south polar regions where the summertime cloud amount over Antarctica is reduced by about 0.05 by the removal of the 3.7-μm channel tests (see discussion below). The average TC are about the same as in ISCCP-D but the PC are generally lower by about 5–15 hPa, the latter produced by the change in atmospheric temperature profiles. Two notable changes are a decrease of TC for ice clouds and high clouds (nearly all ice phase). Although the lowering of the ice phase temperature threshold contributes, most of the decrease in TC is produced by a smaller infrared-to-visible optical thickness ratio in the revised retrieval model, which moves the ice clouds upward (especially over higher-latitude land), despite the downward displacement of the optically thinnest clouds to the tropopause in the tropics and the overall increase of visible optical thickness. The new results are closer to the CALIOP and sounder results (Stubenrauch et al. 2012). In the polar regions, wintertime TC values are warmer by 2–3 K in the H version because of the changed cloud detection logic and the PC values are larger by about 30 hPa because of the atmospheric temperature profile change. Summertime polar TC values are colder in ISCCP-H by about 2 K in the north and about 6 K in the south because of the removal of the 3.7-μm channel tests, which decreases near-surface cloudiness (PC values are lower by 30–50 hPa, respectively). Cloud optical thickness is slightly increased (by about 5% relative), more over land than water: a decrease in values accounting for aerosol effects (which also increases the surface reflectivity slightly) is offset by the overall increase in ice cloud TAU values together with a small increase of liquid cloud TAU values because of the change in assumed droplet size. In the polar regions, TAU is reduced by 10% both because of the aerosols treatment and because of changed ice–liquid definition. Average TS are reduced by about 1 K in the tropics by the changed IR calibration and correction of the near-surface water vapor absorption, offset

by decreased surface emissivities over land, but increased in the polar regions by about 1 K because of the changed IR calibration and decreased surface emissivities. Surface reflectances (RS) are about 1% higher on average because of the aerosol treatment.

ISCCP-H exhibits diurnal variations of CA and other cloud properties that are very similar to ISCCP-D (Rossow and Schiffer 1999, Figs. 4 and 11), including larger amplitudes over land than over oceans and the well-known CA phase difference between land (afternoon peak) and ocean (morning peak). Seasonally (Fig. 3), the summertime CA diurnal amplitudes are larger than the wintertime amplitudes in midlatitudes but smaller in the tropics (as expected). The diurnal behavior of polar clouds (note scale change) is very different between the north, where ocean is surrounded by land, and the south, where land is surrounded by ocean. In the north, the clouds over land show a summertime diurnal behavior similar to the midlatitude land with very little variation over oceans and no variation at all during wintertime. In the south there is little variation in wintertime but during summertime both land and ocean exhibit small diurnal variations but with opposite phases. However, since the longitude coverage in the polar regions is incomplete at each time of day (up to 20% missing near 60°S but as much as 10% over Antarctica), the apparent diurnal variation is caused by the longitudinal rotation of the orbit swaths interacting with longitudinal variations in cloud amount (as shown by *CloudSat–CALIPSO* in Figs. 3 and 4 in Verlinden et al. 2011). The diurnal variations of TAU values in the polar regions (not shown) are much better behaved in the H version than in the previous versions (cf. Fig. 4 in Rossow and Schiffer 1999), exhibiting smaller and better-behaved variations consistent with variations at other latitudes. The only notable change is the summertime cycle of TAU over Antarctica, which exhibits a daytime minimum. The variations of TAU at other latitudes are generally small (<1) but show a hint of solar zenith effects on the retrieval.

Figure 4 shows the seasonal cycles of CA and PC for both poles in two zones that roughly divide land from water. In the north, the ISCCP results show smaller CA in spring (with ocean lagging land by almost two months) and peak CA in autumn–winter; winter CA is roughly similar over ocean and land. *CloudSat–CALIPSO* results show a similar seasonal cycle (systematically more CA as expected) but with somewhat smaller CA in winter than autumn (see Fig. 1 in Liu et al. 2012). That the ISCCP CA is larger over land than ocean in summertime may partially explain the difference noted in earlier studies with surface observations, which are mostly land based. Average PC is smaller in winter and early spring with only small land–water contrast, consistent with *CloudSat–CALIPSO* results that show a significant summer–autumn increase of low clouds relative to higher clouds (see Fig. 13 in Liu et al. 2012). In the south the ocean CA does not vary much seasonally but exhibits a strong variation over Antarctica, smaller in summer and larger in winter. The large land–water contrast and strong seasonality in the southern cloud amounts is confirmed by *CloudSat–CALIPSO* (see Fig. 8 in Bromwich et al. 2012), although the summertime CA reduction caused by the removal of the 3.7-μm tests may have produced an underestimate in ISCCP-H. The average PC is a little larger over ocean
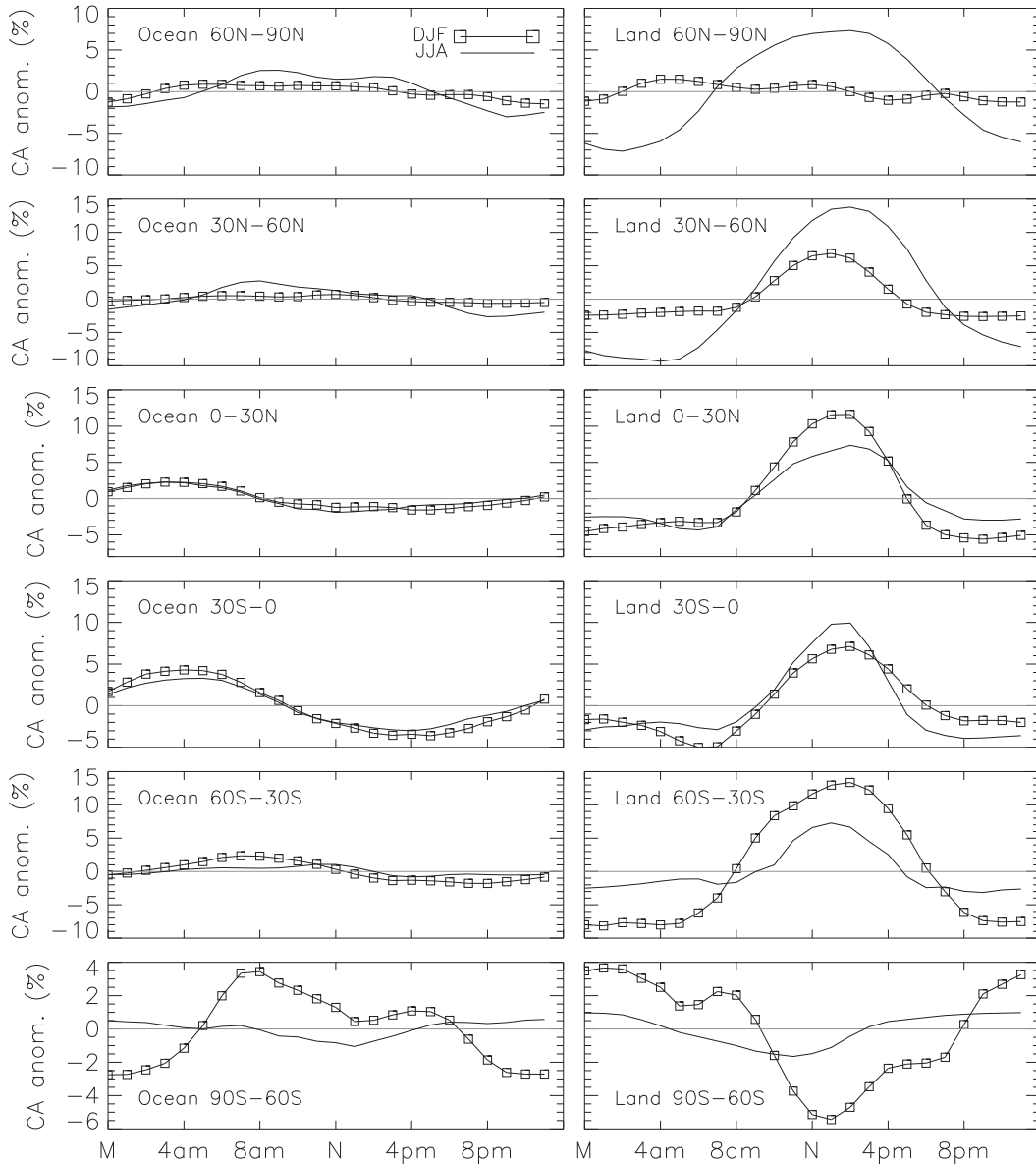
FIG. 3. Average diurnal variations of cloud amount (%) as deviations from daily average in six latitude zones for (left) ocean and (right) land areas, where solid lines are for June–August (JJA) and symbols are for December–February (DJF).

in austral summer and smaller in winter but much smaller over the elevated land with a larger seasonal variation (maximum in summer and minimum in winter–autumn), consistent with *CloudSat–CALIPSO* results (see Fig. 9 in Bromwich et al. 2012). The strong minimum of PC in winter–spring over land suggests that the ISCCP analysis is (partially) detecting the polar stratospheric clouds (see Fig. 9 in Bromwich et al. 2012); if this so, the thinner ones are likely placed at too low in altitude. Figure 3.1.9 in Stubenrauch et al. (2012) shows that the distribution of ISCCP-D TC peaks at larger values (by about 10–15 K) than indicated by CALIOP, so the slightly lower ISCCP-H values are a small improvement. However, the change of atmospheric temperature profiles

used to convert TC to PC produced somewhat larger PC values in winter and smaller values in summer relative to ISCCP-D (by about 30–50 hPa).

The current ISCCP-H record (1983–2018) of monthly anomalies of the global mean cloud properties is shown in Fig. 5 (see Fig. 4 in Young et al. 2018 for a comparison of global mean cloud amounts from ISCCP-D and ISCCP-H for 1983–2009). CA has resumed decreasing after 2011 so that the overall decline in global mean CA is 0.05 from 1987 to 2018 (likely reduced to 0.04 accounting for view-angle effects in the early part of the record, see section 2b); the standard deviation is larger than in ISCCP-D because of the continued downward trend. PC and TC in ISCCP-H are relatively
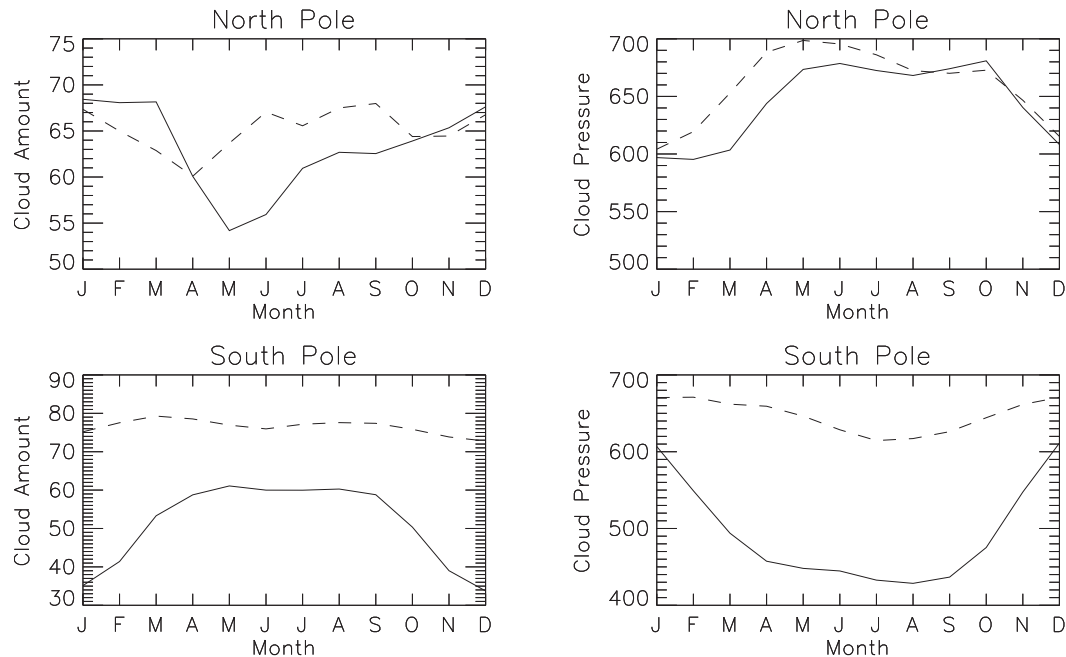
FIG. 4. Average seasonal variations of (left) cloud amount (%) and (right) cloud-top pressure (hPa) as deviations from the annual average in two zones at each pole [(top) north; (bottom) south]: $\pm 60°$–$70°$ (dashed line) and $\pm 70°$–$90°$ (solid line).

constant until 2006 (except for the anomaly in the early 1990s produced by the Mount Pinatubo eruption aerosol, which was not much changed by the correction for stratospheric aerosols, see Luo et al. 2002), when they decrease by about 15 hPa/2 K in 2006–10, after which they increase by 20 hPa/3 K to 2012 and remain constant. The small reduction in the ISCCP-H values in the 1980s may be related to anomalously large humidity values in the NNHIRS product during this period, but TC values offset changes in atmospheric temperature so that PC remains nearly the same. The change of PC later in the record is entirely due to changes in TC, not atmospheric temperature. Optical thickness values are roughly constant, though variable, until about 1998 (with slightly increased values relative to ISCCP-D during the Pinatubo because of the aerosol correction in ISCCP-H), then they increase by about 0.5 until 2006, continue increasing by a similar amount from 2006 to 2012 after a small decrease, and then remain constant. The reduced values after 2006 until 2009, compared to the ISCCP-D, occurred because of a correction to the *NOAA-18* VIS calibration and replacement by *NOAA-19* after 2012. Over the whole record TAU has increased by about 0.5, which may radiatively offset the overall CA decrease: this appears to be the case for the long-term variation of the global-mean solar flux at the top-of-atmosphere, based on ISCCP-FH products (see Zhang_etal_flux-cal_at-iscp_v4_2021.pdf under "FH Documentation and Publications" at https://isccp.giss.nasa.gov/projects/flux.html); however, the global-mean terrestrial flux has increased by 1–2 W m^{-2} (Y.-C. Zhang 2021, personal communication). Loeb et al. (2018) show a small decrease of shortwave flux from around 2012 (also shown in ISCCP-FH, Y.-C. Zhang 2021, personal communication).

The cloud property changes shown in Fig. 5 were investigated to determine which cloud types are contributing to the long-term variation (see Rossow and Schiffer 1999 and Rossow 2017 for definition of types in ISCCP). In terms of their amounts, the dominant cloud types are low [liquid cumulus (Cu) and stratocumulus (Sc)], middle [liquid altocumulus (Ac) and altostratus (As)], and high [ice cirrus (Ci) and cirrostratus (Cs)]. The total CA decrease by 0.05 is accounted for almost entirely by decreases in Cu by 0.02–0.03 (offset by an increase in Sc by 0.01) and Ac by 0.02 with some decrease of Ci by about 0.01. All other cloud-type amounts are constant over the record. The changes in PC/TC and TAU are consistent with these cloud-type changes. Although total CA is not sensitive to changes in radiance calibration, the cloud-type properties are. The changes discussed above cannot be due to a change of VIS calibration because decreases in Cu/Ac/Ci would be associated with corresponding increases in stratus, nimbostratus, and cumulonimbus (St/Ns/Cb). The changes cannot be due to a change of IR calibration because a decrease in Cu would be associated with an increase of Ci (as well as a decrease in St and increase in Cb), which is not observed.

To highlight the value of a lengthening record of cloud variations, we show as an example the differences in the pattern of variations of tropical high-level cloud amount among the different types of ENSO events (see Kao and Yu 2009 for a good overview). Figure 6 shows a Hovmöller plot of the high cloud amount anomalies over the whole ISCCP record with respect to monthly mean values averaged over $\pm 15°$ latitude at each longitude (with an ENSO index). Values shown are 12-month sliding averages, which shifts the timing somewhat. (The vertical band near 60°E longitude is caused
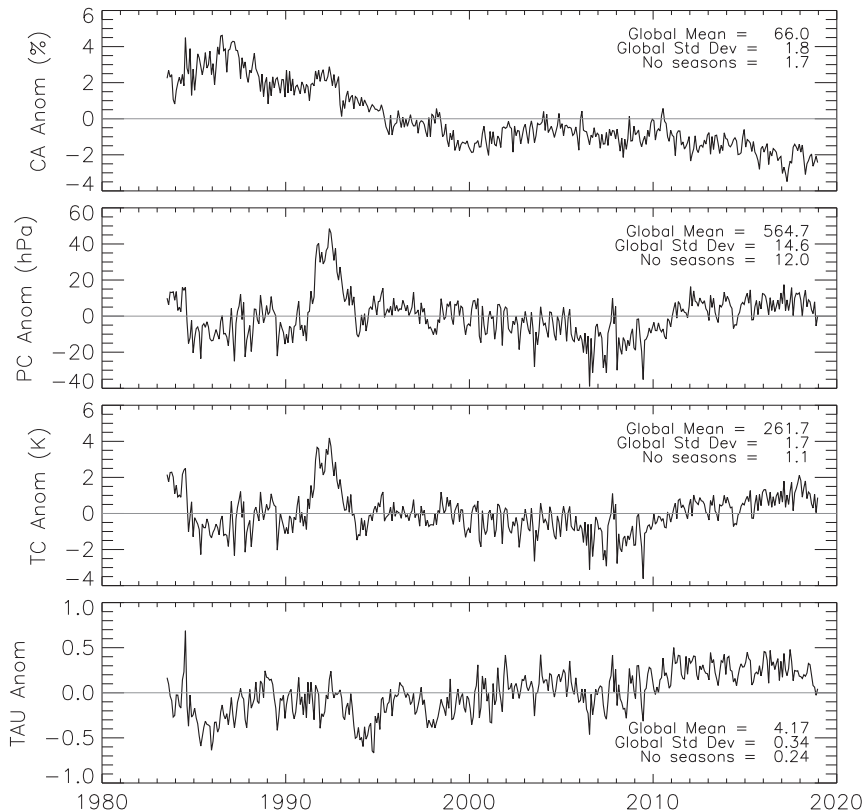
FIG. 5. Anomalies of monthly (deseasonalized) global averages of cloud amount (%), cloud-top pressure (hPa), cloud-top temperature (K), and cloud optical thickness over the whole ISCCP-H record with the mean and the standard deviations with and without seasonal variations shown.

by the lack of geostationary satellite coverage in this sector before 1998.) The "classic" pattern of coincident increases in high cloud amount over the central and eastern Pacific and decreases in the western Pacific during El Niño events are readily seen, especially for the stronger index events in 1985–87, 1997–99, and 2015–17; these variations are followed by reversed anomalies in La Niña events in 1987–90, 1999–2001, and 2017–18. There are two weaker El Niño events in 2003 and 2010 and an unusually extended duration event from 1990 to 1995. That the positive and negative disturbances usually propagate from the eastern Indian Ocean–western Pacific area into the central and eastern Pacific is also apparent; the exceptions being the early 1990s event, where the negative La Niña anomaly does not move into the central-eastern Pacific, and the 1997–99 El Niño, where the positive anomaly appears in the central-eastern Pacific with an unusually strong negative anomaly in the western Pacific (there is just a hint of propagation of the positive anomaly). There are also some occasions (2005–10) where a positive anomaly appears in the western Pacific but does not move beyond the date line; in fact, during this period the positive anomaly appears to move back and forth west of the date line associated with a persistent La Niña index. There is also a suggestion of more frequent high cloud intrusions into the central Pacific

and decreases over the Maritime Continent after about 2006–07. Low cloud westward intrusions into the Maritime Continent area also appear more frequent during this time (not shown). Yu and Kao (2007) noted the occurrence of two kinds of El Niño event, one with elevated temperatures in the central Pacific (CP) and one with elevated temperatures in the east Pacific (EP). Figure 6 does not show any noticeable differences of the high cloud anomalies, but Yu and Kim (2010) note an increased frequency of CP events in the 2000s.

Of all the events in the ISCCP record, only one, 1997–98 [and possibly the event in 2017–18, judging from the cloud variations, but see Paek and Qian (2017)], has been identified (Kao and Yu 2009) as the more usual EP type event; all the others are CP. The latter type has also been divided into three types depending on the way that the warm SST anomaly decays (Yu and Kim 2010): the early 1990s event is a CP with prolonged decay and following EP warming, the 1987–88 event is CP with abrupt decay and following EP cooling, the 1994–95 (end of an extended cloud anomaly) and early 2000s events decay symmetrically with the EP warming. The high cloud amount anomalies shown in Fig. 6 also appear to be consistent with this characterization. That the cloud variation pattern is also different for these different SST anomaly patterns
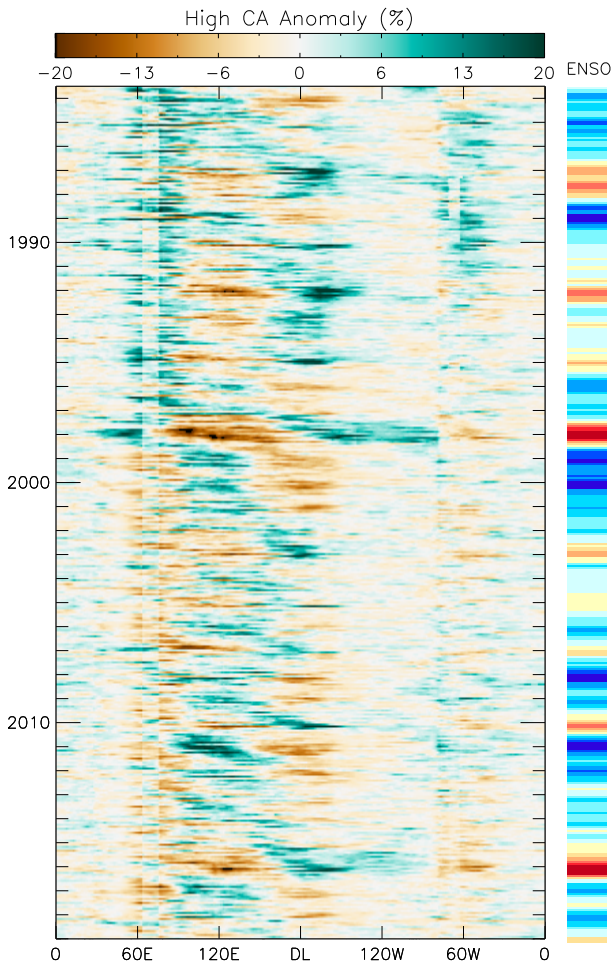
FIG. 6. Hovmöller diagram of time–longitude variations of tropical (averaged over ±15° latitude) monthly mean high cloud amounts as percent deviations from the record average (deseasonalized) at each longitude (green is positive, brown is negative). The ENSO index shown in the bar on the right, where red indicates El Niño and blue indicates La Niña, is based on data from https://origin.cpc.ncep.noaa.gov/products/analysis_monitoring/ensostuff/detrend.nino34.ascii.txt on the NOAA CPC site: https://origin.cpc.ncep.noaa.gov/products/analysis_monitoring/ensostuff/ONI_v5.php.

indicates associated differences in the atmospheric circulation (e.g., Kao and Yu 2009; Gushchina and DeWitte 2012; Chen et al. 2015). More detailed analysis of all the cloud property changes and consequent radiation and precipitation anomalies in atmosphere–ocean energy and water exchanges (like that of Stephens et al. 2018) is warranted.

Investigating the causes of the cloud variations shown in Figs. 5 and 6 (aside from continuing to examine effects of changing satellite characteristics) is still limited by the length of the record, which, despite being 35 years long, is short compared to the PDO and AMO SST variations. In fact, during the entire ISCCP record the PDO has been in its warm phase except for two brief periods 1998–2002 and 2008–12, whereas the AMO has changed from cold to warm phase around 1993

(e.g., Yu et al. 2015). Nevertheless, a detailed diagnosis of the atmosphere–ocean energy exchanges and associated changes in their circulations over this whole period would be very useful in understanding the coupling processes of the climate system (e.g., Zhang et al. 2007).

c. Preliminary uncertainty assessment

The quality results included in ISCCP-H products provide more complete information about the uncertainty in the cloud and surface properties than in ISCCP-D. Two sources of uncertainty are related to the uncertainties in the radiance calibrations (now estimated to be 3% and 1.5 K for VIS and IR, respectively) and to the specific radiative model assumptions used for the cloud and surface retrievals. The former uncertainty translates into uncertainty in the cloud types of about 5% relative to their average amounts (see Fig. 21 in Rossow 2017). The latter effects have not changed the total uncertainty much from ISCCP-D except that the small refinements described may have reduced the bias part of the overall uncertainty.

Instantaneous random retrieval uncertainties are estimated as follows: CA (±0.03), TC (±2 K in the lower atmosphere, ±4 K in the upper atmosphere), PC (±50 hPa in the lower atmosphere, ±100 hPa in the upper atmosphere), TAU (±10%), RS (±5%), and TS (±2 K).

The largest effect on the retrieved results, which can be systematic, is produced by erroneous (false or missed) cloud detections (see discussion in Rossow et al. 1993). This source of uncertainty in all retrieved properties is now reported in each map grid cell every 3 h in terms of the average properties of the clouds that are just barely (marginally) detected by either the VIS or IR or combined radiance tests. On a global monthly average, the "marginal" cloud amount is about 0.1 for an average IR threshold of about 3 K and VIS threshold of 4%. These average values can be used to estimate the magnitude of the changes in the retrieved quantities that would be produced by small changes in the detection threshold, equivalent to the first derivative of the retrieved properties with cloud amount. As discussed in Stubenrauch et al. (2013), different satellite sensors have different cloud detection sensitivities. Based on comparison to the CALIOP observations, the ISCCP cloud detection misses globally about 0.05 of clouds that have TAU values less than about 0.3 and are preferentially located near the tropopause. Some of these clouds are detected only by the IR tests. This bias in total CA implies a high bias in TAU and TC of about 10% and 2 K, respectively. Note that the CA bias nearly offsets the TAU and TC biases in calculations of radiative fluxes (cf. Zhang et al. 1995).

Finally, as the ISCCP retrieval treats each cloud as a single layer, the occurrence of an optically thin cloud overlying lower-level clouds causes the retrieved cloud top in some cases to be biased to larger pressures/temperatures (Jin and Rossow 1997), producing an underestimate of the amount of high cloud and an overestimate of midlevel cloud by about 0.10 (compared to CALIOP results; Stubenrauch et al. 2012, 2013). Because of the difficult observing conditions and small contrast between cloud and clear conditions in the polar regions, the uncertainties of cloud amount and properties in the polar regions are larger than discussed above [e.g., look at the range of

results from different products in Stubenrauch et al. (2012), Liu et al. (2012), Bromwich et al. (2012), and Karlsson and Devasthale (2018)].

5. Conclusions

The ISCCP project is now fully operational: the reduced-resolution radiance images (ISCCP-B1) are sent by the weather satellite operators (currently EUMETSAT, JMA, NOAA) to NCEI. NCEI also collects the operational versions of the ancillary data products (ozone, snow cover, sea ice cover, HIRS atmospheric temperature–humidity profiles). All of these data are processed to produce the ISCCP-H products, currently available from July 1983 through December 2018. A major change now being worked on is to adapt the data from the Visible Infrared Imaging Radiometer Suite (VIIRS) instrument on *NOAA-20*, which has a very different structure from AVHRR, for use in the ISCCP processing. The result will be the VIIRS Global Area Coverage (VGAC), a coarse resolution that matches AVHRR for consistency and can be used by other satellite climate records. Additionally, efforts are ongoing to acquire some older missing imaging data, especially in the early 1980s, to further improve the uniformity of radiance calibrations across the whole record, and make some improvements in the uniformity of the ancillary data products. Once these efforts are completed, the whole record will be reprocessed to produce an even cleaner version and then extended beyond 2018. In the future ISCCP-H will be extended with a lag of 6–18 months, depending on whether or not the reference calibration satellite (afternoon polar) orbiter has changed. NCEI is also working toward development of an interim Climate Data Record (iCDR) to allow more routine production of provisional (with initial calibration) ISCCP-H data.

Regardless of whether the quality and uniformity of the ISCCP products are sufficient for monitoring long-term trends in global cloud properties associated with global warming, the quality is sufficient for examining cloud variations on weather scales to interannual time scales (as shown by the uses to date), so extending the record length serves to provide more examples of the faster variations, such as MJO and ENSO, and begins to provide information about slower variability modes, such as PDO and AMO. Use of ISCCP products to calculate cloud radiative effects is of sufficient quality (Zhang et al. 2004) to study cloud–radiative feedbacks on these interannual variation modes.

An equally important purpose for maintaining the long, uniform ISCCP record is to allow studies to be made with composites of the many other cloud, precipitation, and atmosphere datasets that have collected over the past nearly 40 years from field campaigns and experimental satellite measurements. Although these can provide more detailed information about cloud properties, they generally cover limited time periods and/or spatial domains, often without sufficient time resolution for process studies. However, using the global, 3-h background information provided by the ISCCP products allows for conditional sorting of all of this information (context setting), together with reanalyses, by prevailing cloud and atmospheric conditions. This approach provides context for each experiment that may allow their results to be compared. Some examples of this type of analysis can be found in Oreopoulos and Rossow (2011) for cloud–radiative effects, Rossow et al. (2013) for precipitation, Tselioudis et al. (2013) for cloud vertical structure and atmospheric circulation and Rossow et al. (2016) for diabatic heating of atmosphere (see also the references to other studies in these papers). Tselioudis et al. (2021) use this regime approach to evaluate climate model cloudiness. Many more such studies are possible for cloud-related processes.

To facilitate these developments, the ISCCP processing code (along with an operations guide) is now publicly available. A user's guide to the data products is also available that provides a shorter summary of the detailed documentation in the C-ATBD (Rossow 2017).

REFERENCES

Baran, A. J., and L.-C. Labonnote, 2007: A self-consistent scattering model for cirrus. I: The solar region. *Quart. J. Roy. Meteor. Soc.*, **133**, 1899–1912, https://doi.org/10.1002/qj.164.

Bromwich, D. H., and Coauthors, 2012: Tropospheric clouds in Antarctica. *Rev. Geophys.*, **50**, RG1004, https://doi.org/10.1029/2011RG000363.

Cairns, B., 1995: Diurnal variations of cloud from ISCCP data. *Atmos. Res.*, **37**, 135–146, https://doi.org/10.1016/0169-8095(94)00074-N.

Cao, C.-Y., and A. K. Heidinger, 2002: Inter-comparison of the longwave infrared channels of MODIS and AVHRR/NOAA-16 using simultaneous nadir observations at orbit intersections. *Proc. SPIE*, **4814**, 306, https://doi.org/10.1117/12.451690.

Chen, D., and Coauthors, 2015: Strong influence of westerly wind bursts on El Niño diversity. *Nat. Geosci.*, **8**, 339–345, https://doi.org/10.1038/ngeo2399.

Chen, T., W. B. Rossow, and Y.-C. Zhang, 2000: Radiative effects of cloud-type variations. *J. Climate*, **13**, 264–286, https://doi.org/10.1175/1520-0442(2000)013<0264:REOCTV>2.0.CO;2.

Chowdhary, J., L. D. Travis, and A. A. Lacis, 1995: Incorporation of a rough ocean surface and semi-infinite water body in multiple scattering computations of polarized light in an atmosphere-ocean system. *Proc. SPIE*, **2311**, 58–70, https:// doi.org/10.1117/12.198585.

Clayson, C. A., and A. S. Bogdanoff, 2013: The effect of diurnal sea surface temperature warming on climatological air–sea fluxes. *J. Climate*, **26**, 2546–2556, https://doi.org/10.1175/JCLI-D-12-00062.1.

——, J. B. Roberts, and A. S. Bogdanoff, 2012: The SeaFlux Turbulent Flux dataset version 1.0 documentation. SeaFlux Project, 5 pp., https://seaflux.org/seaflux_data/DOCUMENTATION/SeaFluxDocumentationV12.pdf.

Coopman, Q., J. Riedi, S. Zeng, and T. J. Garrett, 2020: Space-based analysis of the cloud thermodynamic transition for varying microphysical and meteorological regimes. *Geophys. Res. Lett.*, **47**, e2020GL087122, https://doi.org/10.1029/2020GL087122.

Darnell, W. L., S. K. Gupta, W. F. Staylor, N. A. Ritchey, and A. C. Wilber, 1992: Seasonal variation of surface radiation budget derived from the ISCCP C1 data. *J. Geophys. Res.*, **97**, 15 741–15 760, https://doi.org/10.1029/92JD00675.

Doutriaux-Boucher, M., and G. Seze, 1998: Significant changes between the ISCCP C and D cloud climatologies. *Geophys. Res. Lett.*, **25**, 4193–4196, https://doi.org/10.1029/1998GL900081.

Drake, F., 1993: Global cloud cover and cloud water path from ISCCP C2 data. *Int. J. Climatol.*, **13**, 581–605, https://doi.org/10.1002/joc.3370130602.

Evan, A. T., A. K. Heidinger, and D. J. Vimont, 2007: Arguments against a long-term trend in global ISCCP cloud amounts. *Geophys. Res. Lett.*, **14**, L04701, https://doi.org/10.1029/2006GL028083.

Fu, R., A. D. Del Genio, and W. B. Rossow, 1990: Behavior of deep convective clouds in the tropical Pacific deduced from ISCCP radiance data. *J. Climate*, **3**, 1129–1152, https://doi.org/10.1175/1520-0442(1990)003<1129:BODCCI>2.0.CO;2.

Gupta, S. K., N. A. Ritchey, A. C. Wilber, C. H. Whitlock, G. G. Gibson, and P. W. Stackhouse, 1999: A climatology of surface radiation budget derived from satellite data. *J. Climate*, **12**, 2691–2710, https://doi.org/10.1175/1520-0442(1999)012<2691:ACOSRB>2.0.CO;2.

Gushchina, D., and B. DeWitte, 2012: Intraseasonal tropical atmospheric variability associated with the two flavors of El Niño. *Mon. Wea. Rev.*, **140**, 3669–3681, https://doi.org/10.1175/MWR-D-11-00267.1.

Hartmann, D. L., M. E. Ockert-Bell, and M. L. Michelson, 1992: The effect of cloud type on Earth's energy balance: Global analysis. *J. Climate*, **5**, 1281–1304, https://doi.org/10.1175/1520-0442(1992)005<1281:TEOCTO>2.0.CO;2.

Haynes, J. M., C. Jakob, W. B. Rossow, G. Tselioudis, and J. Brown, 2011: Major characteristics of southern ocean cloud regimes and their effects on the energy budget. *J. Climate*, **24**, 5061–5080, https://doi.org/10.1175/2011JCLI4052.1.

Heidinger, A. K., W. C. Straka, C. C. Molling, J. T. Sullivan, and X. Wu, 2010: Deriving an inter-sensor consistent calibration for the AVHRR solar reflectance data record. *Int. J. Remote Sens.*, **31**, 6493–6517, https://doi.org/10.1080/01431161.2010.496472.

Inamdar, A. K., and K. R. Knapp, 2015: Intercomparison of independent calibration techniques applied to the visible channel of the ISCCP B1 data. *J. Atmos. Oceanic Technol.*, **32**, 1225–1240, https://doi.org/10.1175/JTECH-D-14-00040.1.

Intrieri, J. M., M. D. Shupe, T. Uttal, B. J. McCarty, 2002: The annual cycle of Arctic cloud characteristics observed by radar and lidar at SHEBA. *J. Geophys. Res.*, **107**, 8030, https://doi.org/10.1029/2000JC000423.

Jakob, C., and G. Tselioudis, 2003: Objective identifications of cloud regimes in the tropical western Pacific. *Geophys. Res. Lett.*, **30**, 2082, https://doi.org/10.1029/2003GL018367.

——, and C. Schumacher, 2008: Precipitation and latent heating characteristics of the major tropical western Pacific cloud regimes. *J. Climate*, **21**, 4348–4364, https://doi.org/10.1175/2008JCLI2122.1.

——, M. S. Singh, and L. Jungandreas, 2019: Radiative convective equilibrium and organized convection: An observational perspective. *J. Geophys. Res. Atmos.*, **124**, 5418–5430, https://doi.org/10.1029/2018JD030092.

Jin, Y., and W. B. Rossow, 1997: Detection of cirrus overlapping low-level clouds. *J. Geophys. Res.*, **102**, 1727–1737, https://doi.org/10.1029/96JD02996.

Kao, H.-Y., and J.-Y. Yu, 2009: Contrasting eastern-Pacific and central-Pacific types of ENSO. *J. Climate*, **22**, 615–632, https://doi.org/10.1175/2008JCLI2309.1.

Karlsson, K-G., and A. Devasthale, 2018: Inter-comparison and evaluation of the four longest satellite-derived cloud climate data records: CLARA-A2, ESA Cloud CCI V3, ISCCP-HGM, and PATMOS-x. *Remote Sens.*, **10**, 1567, https://doi.org/10.3390/rs10101567.

Kinne, S., and Coauthors, 2013: MAC-v1: A new aerosol climatology for climate studies. *J. Adv. Model. Earth Syst.*, **5**, 704–740, https://doi.org/10.1002/jame.20035.

Knapp, K. R., 2008a: Calibration assessment of ISCCP geostationary infrared observations using HIRS. *J. Atmos. Oceanic Technol.*, **25**, 143–195, https://doi.org/10.1175/2007JTECHA910.1.

——, 2008b: Scientific data stewardship of International Satellite Cloud Climatology Project B1 global geostationary observations. *J. Appl. Remote Sens.*, **2**, 023548, https://doi.org/10.1117/1.3043461.

——, A. H. Young, H. Semunegus, A. K. Inamdar, and W. Hankins, 2021: Adjusting ISCCP cloud detection to increase consistency of cloud amount and reduce artifacts. *J. Atmos. Oceanic Technol.*, **35**, 155–165, https://doi.org/10.1175/JTECH-D-20-0045.1.

Lau, N.-C., and M. W. Crane, 1995: A satellite view of the synoptic-scale organization of cloud properties in midlatitude and tropical circulation systems. *Mon. Wea. Rev.*, **123**, 1984–2006, https://doi.org/10.1175/1520-0493(1995)123<1984:ASVOTS>2.0.CO;2.

Lin, B., and W. B. Rossow, 1996: Seasonal variation of liquid and ice water path in nonprecipitating clouds over oceans. *J. Climate*, **9**, 2890–2902, https://doi.org/10.1175/1520-0442(1996)009<2890:SVOLAI>2.0.CO;2.

Liu, Y., J. R. Key, S. A. Ackerman, G. G. Mace, and Q. Zhang, 2012: Arctic cloud macrophysical characteristics from CloudSat and CALIPSO. *Remote Sens. Environ.*, **124**, 159–173, https://doi.org/10.1016/j.rse.2012.05.006.

Loeb, N. G., T. J. Thorsen, J. R. Norris, H. Wang, and W. Su, 2018: Changes in Earth's energy budget during and after the "pause" in global warming: An observational perspective. *Climate*, **6**, 62, https://doi.org/10.3390/cli6030062.

Luo, Z., and W. B. Rossow, 2004: Characterizing tropical cirrus life cycle, evolution and interaction with upper-tropospheric water vapor using Lagrangian trajectory analysis of satellite observations. *J. Climate*, **17**, 4541–4563, https://doi.org/10.1175/3222.1.

——, ——, T. Inoue, and C. J. Stubenrauch, 2002: Did the eruption of the Mt. Pinatubo volcano affect cirrus properties? *J. Climate*, **15**, 2806–2820, https://doi.org/10.1175/1520-0442(2002)015<2806:DTEOTM>2.0.CO;2.

——, R. C. Anderson, W. B. Rossow, and H. Takahashi, 2017: Tropical cloud and precipitation regimes as seen from near-simultaneous

TRMM, CloudSat and CALIPSO observations and comparison with ISCCP. *J. Geophys. Res. Atmos.*, **122**, 5988–6003, https://doi.org/10.1002/2017JD026569.

Mace, G. G., Q. Zhang, M. Vaughan, R. Marchand, G. Stephens, C. Trepte, and D. Winker, 2009: A description of hydrometeor layer occurrence statistics derived from the first year of merged CloudSat and CALIPSO data. *J. Geophys. Res.*, **114**, D00A26, https://doi.org/10.1029/2007JD009755.

Machado, L. A. T., W. B. Rossow, R. L. Guedes, and A. W. Walker, 1998: Life cycle variations of mesoscale convective systems over the Americas. *Mon. Wea. Rev.*, **126**, 1630–1654, https://doi.org/10.1175/1520-0493(1998)126<1630:LCVOMC>2.0.CO;2.

Marchand, R., T. Ackerman, M. Smyth, and W. B. Rossow, 2010: A review of cloud top height and optical depth histograms from MISR, MODIS, and ISCCP. *J. Geophys. Res.*, **115**, D16206, https://doi.org/10.1029/2009JD013422.

Mekonnen, A., and W. B. Rossow, 2011: The interaction between deep convection and easterly waves tropical North Africa: A weather state perspective. *J. Climate*, **24**, 4276–4294, https://doi.org/10.1175/2011JCLI3900.1.

——, and ——, 2018: The interaction between cloud regimes and easterly wave activity over Africa: Convective transitions and mechanisms. *Mon. Wea. Rev.*, **146**, 1945–1961, https://doi.org/10.1175/MWR-D-17-0217.1.

Molling, C. C., A. K. Heidinger, W. C. Straka, and X. Wu, 2010: Calibrations for AVHRR channels 1 and 2: Review and path towards consensus. *Int. J. Remote Sens.*, **31**, 6419–6540, https://doi.org/10.1080/01431161.2010.496473.

Naszaryan, H., M. P. McCormick, and W. P. Menzel, 2008: Global characterization of cirrus clouds using CALIPSO data. *J. Geophys. Res.*, **113**, D16211, https://doi.org/10.1029/2007JD009481.

Oreopoulos, L., and W. B. Rossow, 2011: The cloud radiative effect of ISCCP weather states. *J. Geophys. Res.*, **116**, D12202, https://doi.org/10/1029/2010jd015472.

Paek, H., J.-Y. Yu, and C. Qian, 2017: Why were the 2015/2016 and 1997/1998 extreme El Niños different? *Geophys. Res. Lett.*, **44**, 1848–1856, https://doi.org/10.1002/2016GL071515.

Polly, J., and W. B. Rossow, 2016: Distribution of midlatitude cyclone attributes based on the MCMS database. *J. Climate*, **29**, 6483–6507, https://doi.org/10.1175/JCLI-D-15-0857.1.

Pope, M., C. Jakob, and M. J. Reeder, 2009a: Objective classification of tropical mesoscale convective systems. *J. Climate*, **22**, 5797–5808, https://doi.org/10.1175/2009JCLI2777.1.

——, ——, and ——, 2009b: Regimes of the north Australian wet season. *J. Climate*, **22**, 6699–6715, https://doi.org/10.1175/2009JCLI3057.1.

Raschke, E., S. Kinne, W. B. Rossow, P. W. Stackhouse, and M. Wild, 2016: Comparison of radiative energy flows in observational datasets and climate modeling. *J. Appl. Meteor. Climatol.*, **55**, 93–117, https://doi.org/10.1175/JAMC-D-14-0281.1.

Riedi, J., and Coauthors, 2010: Cloud thermodynamic phase inferred from merged POLDER and MODIS data. *Atmos. Chem. Phys.*, **10**, 11 851–11 865, https://doi.org/10.5194/acp-10-11851-2010.

Rossow, W. B., 2017: ISCCP Cloud Properties—H-Series Product. NOAA Climate Data Record Program Doc. CDRP-ATDB-0.872, 301 pp., http://www1.ncdc.noaa.gov/pub/data/sds/cdr/CDRs/Cloud_Properties-ISCCP/AlgorithmDescription_01B-29.pdf.

——, and R. A. Schiffer, 1991: ISCCP cloud data products. *Bull. Amer. Meteor. Soc.*, **72**, 2–20, https://doi.org/10.1175/1520-0477(1991)072<0002:ICDP>2.0.CO;2.

——, and L. C. Garder, 1993a: Cloud detection using satellite measurements of infrared and visible radiances for ISCCP. *J. Climate*, **6**, 2341–2369, https://doi.org/10.1175/1520-0442(1993)006<2341:CDUSMO>2.0.CO;2.

——, and ——, 1993b: Validation of ISCCP cloud detections. *J. Climate*, **6**, 2370–2393, https://doi.org/10.1175/1520-0442(1993)006<2370:VOICD>2.0.CO;2.

——, and B. Cairns, 1995: Monitoring changes of clouds. *Climatic Change*, **31**, 305–347, https://doi.org/10.1007/BF01095151.

——, and Y.-C. Zhang, 1995: Calculation of surface and top-of-atmosphere radiative fluxes from physical quantities based on ISCCP datasets, Part II: Validation and first results. *J. Geophys. Res.*, **100**, 1167–1197, https://doi.org/10.1029/94JD02746.

——, and R. A. Schiffer, 1999: Advances in understanding clouds from ISCCP. *Bull. Amer. Meteor. Soc.*, **80**, 2261–2287, https://doi.org/10.1175/1520-0477(1999)080<2261:AIUCFI>2.0.CO;2.

——, and J. Ferrier, 2015: Evaluation of long-term calibrations of the AVHRR visible radiances. *J. Atmos. Oceanic Technol.*, **32**, 744–766, https://doi.org/10.1175/JTECH-D-14-00134.1.

——, and J. J. Bates, 2019: Building an accessible, integrated Earth observing and information system: The International Satellite Cloud Climatology Project as a pathfinder. *Bull. Amer. Meteor. Soc.*, **100**, 2423–2431, https://doi.org/10.1175/BAMS-D-19-0060.1.

——, and Coauthors, 1985: ISCCP cloud algorithm intercomparison. *J. Climate Appl. Meteor.*, **24**, 877–903, https://doi.org/10.1175/1520-0450(1985)024<0887:ICAI>2.0.CO;2.

——, A. W. Walker, and L. C. Garder, 1993: Comparison of ISCCP and other cloud amounts. *J. Climate*, **6**, 2394–2418, https://doi.org/10.1175/1520-0442(1993)006<2394:COIAOC>2.0.CO;2.

——, Y.-C. Zhang, and J.-H. Wang, 2005a: A statistical model of cloud vertical structure based on reconciling cloud layer amounts inferred from satellites and radiosonde humidity profiles. *J. Climate*, **18**, 3587–3605, https://doi.org/10.1175/JCLI3479.1.

——, G. Tselioudis, A. Polak, and C. Jakob, 2005b: Tropical climate described as a distribution of weather states indicated by distinct mesoscale cloud property mixtures. *Geophys. Res. Lett.*, **32**, L21812, https://doi.org/10.1029/2005GL024584.

——, A. Mekonnen, C. Pearl, and W. Goncalves, 2013: Tropical precipitation extremes. *J. Climate*, **26**, 1457–1466, https://doi.org/10.1175/JCLI-D-11-00725.1.

——, Y.-C. Zhang, and G. Tselioudis, 2016: Atmospheric diabatic heating in different weather states and the general circulation. *J. Climate*, **29**, 1059–1065, https://doi.org/10.1175/JCLI-D-15-0760.1.

Schiffer, R. A., and W. B. Rossow, 1983: The International Satellite Cloud Climatology Project (ISCCP): The first project of the World Climate Research Programme. *Bull. Amer. Meteor. Soc.*, **64**, 779–784, https://doi.org/10.1175/1520-0477-64.7.779.

——, and ——, 1985: ISCCP global radiance data set: A new resource for climate research. *Bull. Amer. Meteor. Soc.*, **66**, 1498–1505, https://doi.org/10.1175/1520-0477(1985)066<1498:IGRDSA>2.0.CO;2.

Stephens, G. L., and Coauthors, 2018: Regional intensification of tropical hydrological cycle during ENSO. *Geophys. Res. Lett.*, **45**, 4361–4370, https://doi.org/10.1029/2018GL077598.

Stramler, K., A. D. Del Genio, and W. B. Rossow, 2011: Synoptically driven Arctic winter states. *J. Climate*, **24**, 1747–1762, https://doi.org/10.1175/2010JCLI3817.1.

Stubenrauch, C. J., W. B. Rossow, F. Cheruy, A. Chedin, and N. A. Scott, 1999: Clouds as seen by satellite sounders (3I) and imagers (ISCCP). Part I: Evaluation of cloud parameters. *J. Climate*,

12, 2189–2213, https://doi.org/10.1175/1520-0442(1999)012<2189:CASBSS>2.0.CO;2.

——, ——, and S. Kinne, 2012: Assessment of global cloud datasets from satellites: A project of the World Climate Research Programme Global Energy and Water Cycle Experiment (GEWEX) Radiation Panel. WCRP Rep. 23/2012, 176 pp., https://www.wcrp-climate.org/documents/GEWEX_Cloud_Assessment_2012.pdf.

——, and Coauthors, 2013: Assessment of global cloud datasets from satellites: Project and database initiated by the GEWEX Radiation Panel. *Bull. Amer. Meteor. Soc.*, **94**, 1031–1049, https://doi.org/10.1175/BAMS-D-12-00117.1.

Sun, Y., and Y. Huang, 2018: An examination of convective moistening of the lower stratosphere using satellite data. *Earth Space Sci.*, **2**, 320–330, https://doi.org/10.1002/2015EA000115.

Tan, J., and C. Jakob, 2013: A three-hourly dataset of the state of tropical convection based on cloud regimes. *Geophys. Res. Lett.*, **40**, 1415–1419, https://doi.org/10.1002/grl.50294.

——, ——, W. B. Rossow, and G. Tselioudis, 2015: The role of organized deep convection in explaining observed tropical rainfall changes. *Nature*, **519**, 451–454, https://doi.org/10.1038/nature14339.

Tian, B., D. E. Waliser, and E. J. Fetzer, 2006: Modulation of the diurnal cycle of tropical deep convective clouds by the MJO. *Geophys. Res. Lett.*, **33**, L20704, https://doi.org/10.1029/2006GL027752.

Tromeur, E., and W. B. Rossow, 2010: Interaction of tropical deep convection with the large-scale circulation in the Madden–Julian oscillation. *J. Climate*, **23**, 1837–1853, https://doi.org/10.1175/2009JCLI3240.1.

Tselioudis, G., Y.-C. Zhang, and W. B. Rossow, 2000: Cloud and radiation variations associated with northern midlatitude low and high sea level pressure regimes. *J. Climate*, **13**, 312–327, https://doi.org/10.1175/1520-0442(2000)013<0312:CARVAW>2.0.CO;2.

——, E. Tromeur, W. B. Rossow and C. S. Zerefos, 2010: Decadal changes in tropical convection and possible effects on stratospheric water vapor. *Geophys. Res. Lett.*, **37**, L14806, https://doi.org/10.1029/2010GL044092.

——, W. B. Rossow, Y.-C. Zhang, and D. Konsta, 2013: Global weather states and their properties from passive and active satellite cloud retrievals. *J. Climate*, **26**, 7734–7746, https://doi.org/10.1175/JCLI-D-13-00024.1.

——, B. R. Lipat, D. Konsta, K. M. Grise, and L. M. Polvani, 2016: Midlatitude cloud shifts, their primary link to the Hadley cell, and their diverse radiative effects. *Geophys. Res. Lett.*, **43**, 4594–4601, https://doi.org/10.1002/2016GL068242.

——, W. B. Rossow, C. Jakob, J. Remillard, D. Tropf, and Y.-C. Zhang, 2021: Evaluation of clouds, radiation, and precipitation in CMIP6 models using global weather states derived from ISCCP-H cloud property data. *J. Climate*, **34**, 7311–7324, https://doi.org/10.1175/JCLI-D-21-0076.1.

Verlinden, K. L., D. W. J. Thompson, and G. L. Stephens, 2011: The three-dimensional distribution of clouds over the southern hemisphere high latitudes. *J. Climate*, **24**, 5799–5811, https://doi.org/10.1175/2011JCLI3922.1.

Wang, J., W. B. Rossow, and Y.-C. Zhang, 2000: Cloud vertical structure and its variations from a 20-year global rawinsonde dataset. *J. Climate*, **13**, 3041–3056, https://doi.org/10.1175/1520-0442(2000)013<3041:CVSAIV>2.0.CO;2.

Winker, D. M., M. A. Vaughan, A. Omar, Y. Hu, and K. A. Powell, 2009: Overview of the CALIPSO mission and CALIOP data processing algorithms. *J. Atmos. Oceanic Technol.*, **26**, 2310–2323, https://doi.org/10.1175/2009JTECHA1281.1.

Worku, L. Y., A. Mekonnen, and C. J. Schreck, 2019: Diurnal cycle of rainfall and convection over Maritime Continent using TRMM and ISCCP. *Int. J. Climatol.*, **39**, 5191–5200, https://doi.org/10.1002/joc.6121.

——, ——, and ——, 2020: The impact of MJO, Kelvin, equatorial Rossby waves on the diurnal cycle over the Maritime Continent. *Atmosphere*, **11**, 711, https://doi.org/10.3390/atmos11070711.

Young, A. H., K. R. Knapp, A. Inamdar, W. Hankins, and W. B. Rossow, 2018: The International Satellite Cloud Climatology Project H-Series climate data record product. *Earth Syst. Sci. Data*, **10**, 583–593, https://doi.org/10.5194/essd-10-583-2018.

Yu, J.-Y., and H.-Y. Kao, 2007: Decadal changes of ENSO persistence barrier in SST and ocean heat content indices: 1958-2001. *J. Geophys. Res.*, **112**, D13106, https://doi.org/10.1029/2006JD007654.

——, and S. T. Kim, 2010: Three evolution patterns of central-Pacific El Niño. *Geophys. Res. Lett.*, **37**, L08706, https://doi.org/10.1029/2010GL042810.

——, P.-K. Kao, H. Paek, H.-H. Hsu, C.-W. Hung, M.-M. Lu, and S.-I. An, 2015: Linking emergence of central Pacific El Niño to Atlantic multidecadal oscillation. *J. Climate*, **28**, 651–662, https://doi.org/10.1175/JCLI-D-14-00347.1.

Zhang, B., Z. Guo, L. Zhang, T. Zhou, and T. Hayasaya, 2020: Cloud characteristics and radiative forcing in the global land monsoon region from multisource satellite data sets. *Earth Space Sci.*, **7**, e2019ea001027, https://doi.org/10.1029/2019EA001027.

Zhang, M. H., and Coauthors, 2005: Comparing clouds and their seasonal variation in 10 atmospheric general circulation models with satellite measurements. *J. Geophys. Res.*, **110**, D15S02, https://doi.org/10.1029/2004JD005021.

Zhang, Y.-C., W. B. Rossow, and A. A. Lacis, 1995: Calculation of surface and top-of-atmosphere radiative fluxes from physical quantities based on ISCCP datasets. Part I: Method and sensitivity to input data uncertainties. *J. Geophys. Res.*, **100**, 1149–1165, https://doi.org/10.1029/94JD02747.

——, ——, ——, M. I. Mishchenko, and V. Oinas, 2004: Calculation of radiative fluxes from the surface to top-of-atmosphere based on ISCCP and other global datasets: Refinements of the radiative transfer model and the input data. *J. Geophys. Res.*, **109**, D19105, https://doi.org/10.1029/2003JD004457.

——, ——, P. Stackhouse, A. Romanou, and B. A. Wielicki, 2007: Decadal variations of global energy and ocean heat budget and meridional energy transports inferred from recent global data sets. *J. Geophys. Res.*, **112**, D22101, https://doi.org/10.1029/2007JD008435.